

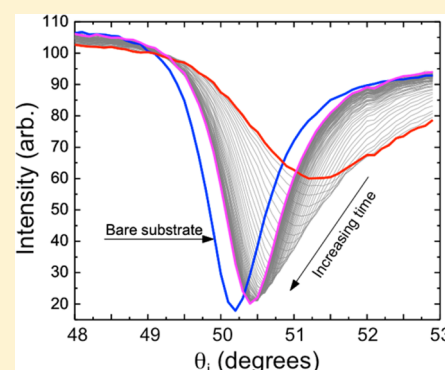
Advances in Surface Plasmon Resonance Imaging Enable Quantitative Tracking of Nanoscale Changes in Thickness and Roughness

Adam N. Raegen,[†] Kyle Reiter,[†] Alexander Dion,[†] Anthony J. Clarke,[‡] Jacek Lipkowski,[§] and John R. Dutcher^{*,†}

[†]Department of Physics, [‡]Department of Molecular and Cellular Biology, and [§]Department of Chemistry, University of Guelph, Guelph, ON, Canada N1G 2W1

S Supporting Information

ABSTRACT: To date, detailed studies of the thickness of coatings using surface plasmon resonance have been limited to samples that are very uniform in thickness, and this technique has not been applied quantitatively to samples that are inherently rough or undergo instabilities with time. Our manuscript describes a significant improvement to surface plasmon resonance imaging (SPRi) that allows this sensitive technique to be used for quantitative tracking of the thickness and roughness of surface coatings that are rough on the scale of tens of nanometers. We tested this approach by studying samples with an idealized, one-dimensional roughness: patterned channels in a thin polymer film. We find that a novel analysis of the SPRi data collected with the plane of incidence parallel to the patterned channels allows the determination of the thickness profile of the channels in the polymer film, which is in agreement with that measured using atomic force microscopy. We have further validated our approach by performing SPRi measurements perpendicular to the patterned channels, for which the measured SPR curve agrees well with the single SPR curve calculated using the average thickness determined from the thickness profile as determined using AFM. We applied this analysis technique to track the average thickness and RMS roughness of cellulose microfibrils upon exposure to cellulolytic enzymes, providing quantitative determinations of the times of action of the enzymes that are of direct interest to the cellulosic ethanol industry.



The surface plasmon resonance (SPR) phenomenon is routinely used to probe the adsorption of molecules onto surfaces.^{1–4} SPR measurements exploit the excitation of a collective oscillation of conduction electrons in thin metallic (typically gold or silver) films^{5,6} or nanoparticles^{7–10} by incident light, referred to as the surface plasmon resonance. The electric field of the surface plasmon decays exponentially into the surrounding media, which allows the adsorption of molecules onto the metallic surface to be monitored through shifts in the SPR condition. To couple the light into the surface plasmon in a thin metallic film, it is necessary to use, for example, a coupling surface grating or a high index glass prism. In the Kretschmann-Raether geometry,³ the light is directed onto the metal film through a high index glass prism, reflecting from the glass/metal interface, and the intensity of the reflected light is measured. The surface plasmon resonance condition is identified experimentally by varying either the wavelength λ of the light or the angle of incidence θ_i to find the value that corresponds to the minimum in the reflected intensity. In the case of varying θ_i , the plot of reflected intensity versus θ_i is referred to as the SPR curve, which exhibits a dip (SPR dip) characterized by the angular position and intensity of the SPR minimum and an associated width.

The SPR technique is used extensively in biosensing applications to determine if biomolecules of interest bind to a biofunctionalized sensor surface, and to determine the kinetics of binding.^{1,11} For this type of SPR measurement, a fixed value of θ_i is typically used, with a value near the SPR minimum or at the inflection point on the low angle side of the minimum,⁴ and changes in the reflected light intensity associated with the adsorption of the biomolecules are measured. It is also possible to measure the SPR curve using angle-scanning SPR techniques. Most previous studies using angle-scanning SPR measured either a small area or a narrow line on the sample, depending on the symmetry of the prism used (e.g. hemispherical or cylindrical).¹² The measured SPR curves were then analyzed to determine the angular position of the SPR minimum, as in refs 5, 13, and 14. There have been limited investigations into changes to the shape or depth of the SPR dip, often attributing any changes to a larger effective thickness or changes to the refractive indices due to the presence of roughness¹⁵ or nanoparticles.^{7–10}

Received: October 25, 2013

Accepted: March 9, 2014

By replacing the photodetector by a CCD camera and using an expanded, collimated incident beam of light in the SPR experiment, the sample surface can be imaged, allowing simultaneous monitoring of the SPR condition on small, biofunctionalized regions. In this way, SPR imaging (SPRi) can be used for high throughput screening of biomolecular binding.^{1,4} In this implementation of the SPRi technique, it is necessary to use small (typically hundreds of micrometers on a side), uniformly coated regions on the sample surface, since the measurements for each region are interpreted in terms of models that incorporate layers having parallel interfaces and uniform properties to represent the different components of the sample (high index glass, thin gold layer, sample film, and surrounding medium). Within the context of such a multilayer model, SPR curves can be calculated using the Fresnel equations,^{3,16} which account for the indices of refraction and uniform thicknesses of the different layers within the multilayer geometry.

Although films are never perfectly smooth, it is possible to deposit films using vacuum deposition, spin-coating, and self-assembly techniques such that the films have subnanometer root-mean-square (RMS) roughness over large lateral length scales. These films are sufficiently smooth to be adequately described by layers with uniform thickness and index of refraction. However, many materials are not amenable to these specialized film deposition techniques. In addition, smooth films can undergo instabilities (e.g. dewetting, in response to changes in environmental conditions). In both cases, the films do not meet the daunting roughness criterion and cannot be considered smooth. The challenge that is addressed in the present study is to extend the SPRi technique to allow the quantitative measurement of the average thickness and roughness of samples having thickness variations of tens of nanometers occurring over lateral length scales of micrometers (rough films or nonuniform coatings). Given the high sensitivity of the SPR technique, with the ability to measure changes in uniform film thickness at the subnanometer level, it is clear that uniform slab models will not be adequate to describe rough films. It is necessary to go beyond the conventional analysis method, by accounting for spatial variations in thickness and index of refraction within the film, such that an adequate description is obtained of the detailed shape of the entire SPR curve.

In the present work, we extend the capabilities of SPRi to obtain quantitative information on rough films. Since modeling of these samples by uniform layers does not work, even if we represent them as an effective medium (e.g., Maxwell-Garnett),^{7,9} we have instead modeled the rough films as consisting of a linear combination of uniform layers of different thickness, similar to the approach of Fenstermaker and McCrackin.¹⁷ By varying the relative weighting of the different layers, the average thickness and roughness of a real sample can be described.

We tested this approach using samples with a well-defined, one-dimensional roughness: patterned channels in polymer films spin-coated onto thin gold films. By performing SPRi measurements with the plane of incidence parallel to the channels within the film, we obtained excellent fits of the measured SPR curves with a thickness profile that agrees closely with that measured using atomic force microscopy (AFM). We have further validated this approach by performing SPRi measurements with the plane of incidence perpendicular to the channels within the film. For this geometry, we obtained

excellent agreement between the measured SPR curves and those calculated using the average thickness of the samples as determined by AFM.

After validating our approach on samples with idealized roughness, we used this technique to measure the thickness and roughness of samples consisting of cellulose microfibrils deposited onto thioglucose-coated thin gold films. This is an example of a sample that is inherently rough because it is made up of many randomly oriented cellulose microfibrils deposited onto the underlying gold surface. Such samples are of great interest to the cellulosic ethanol industry since they allow the measurement of the kinetics of degradation of real cellulose fibers by cellulolytic enzymes. By introducing cellulolytic enzymes into the SPRi liquid cell, we were able to track the time evolution of the average thickness and RMS roughness of the cellulose microfibril samples, providing quantitative determinations of the times of action of the enzymes. This advance in SPRi instrumentation and data analysis opens up new possibilities to track the time evolution of film morphology with nanometer resolution.

MATERIALS AND METHODS

Preparation of SPR Substrates. SPR substrates, which are SF-10 glass slides coated with a thin gold layer (~ 45 nm thick), were purchased from GWC Technologies, Inc. and then cleaned with ethanol before use. For use in subsequent experiments, the gold film was removed from the glass substrate and redeposited using the following procedure. The substrate was wiped with optical lens paper soaked in ethanol. The gold film was removed by placing the substrate for 1 h in aqua regia as it was heated to just below the boiling point (note: the treatment using heated aqua regia was performed in a fume hood for safety reasons). The slide was then rinsed in copious amounts of ultrapure Milli-Q water (resistivity of 18.2 M Ω -cm; note that only ultrapure Milli-Q water was used in the present study) and then sonicated in a heated 1:1 mixture of chloroform and ethanol for 5 min. The slide was then rinsed in both ethanol and water, sonicated in ethanol for 5 min, and then sonicated for 5 min three times in water, rinsing with water between each step. The slide was stored under ethanol prior to the deposition of the metallic films.

A home-built thermal evaporation system (base pressure of $\sim 10^{-6}$ Torr) was used to deposit a very thin (~ 3 nm thick) titanium adhesion layer on the cleaned SF-10 glass slide, followed by a thicker (~ 45 nm thick) gold layer. The thicknesses of the metal layers were monitored during deposition using a quartz crystal microbalance.

Preparation of Patterned PMMA Films. A thin film of poly(methyl methacrylate) (PMMA, molecular weight $M_w = 1540$ k, polydispersity $M_w/M_n = 1.40$) was spincoated directly onto a SPR substrate using a solution of PMMA in toluene (1% by mass) and a spin speed of 2000 rpm. This resulted in a PMMA film that was 48 nm thick. Electron beam lithography was used to expose regions of the PMMA films within an FEI Inspect S50 scanning electron microscope (SEM) (voltage of 10 kV, magnification of 800 \times , 60 μ s raster time, 20 s exposure per channel) by rastering the beam across small regions of the sample. Two different types of regions in the PMMA film were fabricated: a region in which the PMMA film was uniformly exposed in a large 340 \times 400 μ m rectangular area, and regions that contained a periodic array of ~ 5 μ m wide lines with a period of 20 μ m patterned into the PMMA film. The exposed PMMA film was then developed by exposure to a 1:3 mixture

of methyl-isobutyl ketone and isopropanol for 1 min, followed by rinsing with ethanol and water to remove the exposed regions of the films. This resulted in samples that contained three types of regions: unpatterned regions that were uniformly coated with PMMA, regions in which the PMMA had been uniformly removed that were used to characterize the underlying gold layer ("bare gold" layer), and regions that contained one-dimensional patterned channels in the PMMA film.

Preparation of Cellulose Microfibril Suspensions and Cellulose-Coated Substrates. The cellulose microfibrils used in the enzymatic degradation experiment were produced by the bacterium *Gluconacetobacter xylinum*, following a procedure that was similar to that described in ref 18. To prepare the cellulose fibers for deposition onto the substrate, they were ball-milled in HPLC-grade methanol. To separate the cellulose from contaminants, the cellulose suspension was centrifuged at 870g, 1540g, and 1950g for 3 min each. After each centrifugation, excess methanol was removed, more methanol was added, and the cellulose was resuspended by vortexing the mixture for 1 min. Chloroform was subsequently added to the suspension to achieve a mixture of 7:3 chloroform:methanol by volume, which increased the rate of evaporation after the suspension was deposited onto the water surface of a Langmuir trough.

To promote adhesion of the cellulose microfibrils to the SPR substrates, a self-assembled monolayer (SAM) of thioglucose was deposited onto the gold-coated slides by placing the slides in a dilute (~2%) solution of 1-thio-D-glucose (Sigma-Aldrich) in spectroscopic-grade methanol (Fisher Scientific) for >16 h.¹⁹ Cellulose microfibrils were then deposited onto the thioglucose-coated slides using Langmuir–Blodgett deposition at a surface pressure of 5 mN/m using a KSV NIMA Langmuir trough. Slides were stored in a humid environment until they were placed in the SPR sample cell immediately prior to measurement. Similar samples were used in complementary, high-resolution atomic force microscopy (AFM) measurements of enzymatic degradation of the cellulose microfibrils.^{18,20}

Preparation of Buffer and Enzyme Solutions. Sodium citrate buffer (50 mM, pH 5.4) was prepared with 0.2286 g of citric acid and 1.121 g of sodium citrate in 100 mL of water. The *Trichoderma reesei* cellulolytic enzyme cocktail was purchased in the lyophilized form from Sigma-Aldrich (Sigma part number C8546) and dissolved to 200 $\mu\text{g/mL}$ in citrate buffer. The cellobiohydrolase CBH2 enzyme was separated from a commercial *Trichoderma reesei* cellulase secretome by Iogen Corporation and tested for the presence of other major cellulases by performing a Western Blot analysis. The CBH2 enzyme was provided in the frozen state in pH 5.0, 50 mM citrate buffer, and diluted (126 $\mu\text{g/mL}$) 1 mL aliquots were stored in the frozen state. Buffer (0.45 mL for the enzyme cocktail experiment and 0.50 mL for the CBH2 experiment) was injected into the fluid cells using a 1 mL disposable tuberculin syringe (Fisher). While running the experiment for 30–60 min to allow equilibration of the temperature at 50 °C, an aliquot of enzyme solution was heated to the same temperature. The enzyme solution (0.05 mL for the enzyme cocktail experiment and 0.10 mL for the CBH2 experiment) was then added to the fluid cell to achieve the final desired concentrations of 20 $\mu\text{g/mL}$ for the enzyme cocktail and 21 $\mu\text{g/mL}$ for CBH2.

SPR Experimental and Data Analysis Procedures. Angle-scanning SPR imaging (SPRi) experiments were

performed using a custom-modified instrument that is based on the SPRImager (GWC Technologies, Inc.),⁶ with several refinements that are described below and in ref 6. The instrument uses the Kretschmann–Raether geometry, exploiting the internal reflection of light from a gold-coated SF-10 (index of refraction $n = 1.71126$ at $\lambda = 794.7$ nm) glass slide through an intervening triangular SF-10 prism (apex angle of 60°), which was index-matched to the glass slide using a thin layer of index-matching fluid (index of refraction $n = 1.720$ at $\lambda = 589.3$ nm, R.P. Cargille Laboratories). Illumination of the sample at an angle of incidence θ_i was provided by a collimated, ~2.5 cm diameter white light beam that passed through a rotatable polarizer that allowed the use of either *p*- or *s*-polarized light. The light reflected from the sample passed through a narrow bandpass filter ($\lambda = 794.7$ nm, FWHM 1.5 nm, Melles Griot) and was directed onto a CCD camera (Watek). The sample stage and detector arm were rotated in a θ – 2θ configuration using RS-232 computer-controlled rotation stages (RT-3, Newmark Systems), with each angle value determined to within $\pm 0.02^\circ$.

The spatial resolution of the SPRi measurement can be understood as follows. The light beam illuminating the sample is ~2.5 cm in diameter, and the sample substrate beneath the glass coupling prism is also ~2.5 cm on a side. Due to refraction and foreshortening effects, the footprint of the beam in the plane of incidence is ~2 cm. The edges of the sample were not imaged, as they were not in contact with fluid. This means that our 752 \times 480 pixel camera images correspond to a sample area of ~1.5 \times 2 cm, with each pixel corresponding to a sample area of ~19 \times 40 μm . ROIs were chosen to be typically ~12 \times 4 pixels, with the 420 μm long lines in the patterned substrates ~11 pixels or ~21 pixels, depending on the orientation.

A custom data collection and analysis program was used to correct for the translation and foreshortening of multiple regions of interest (ROIs) that occurred as the value of θ_i was varied.^{6,21} By applying this procedure, multiple ROIs could be defined at one value of θ_i and then tracked accurately as θ_i was varied. A time series of SPR images was collected during angle scanning, with a time resolution of ~1 s per image and the value of θ_i corresponding to each image measured precisely. This allowed the calculation of the average intensity within each ROI as a function of θ_i . From these measurements, we were able to determine typical kinetics data (time dependence of reflectivity measured at a fixed value of θ_i), as well as the evolution with time of the entire SPR curve, which provided information on the width, depth, and angular position of the SPR minimum, as well as substructure within the SPR dip.

The SPR sample stage consisted of three separate chambers that were sealed with a Viton rubber gasket against the SPR substrate. The chambers were filled with fluid, either water or aqueous buffer. The stage was placed on the motor assembly and the angle of incidence θ_i was set to 50°, corresponding roughly to the angular position of the SPR minimum for a bare substrate, for the materials and wavelength used in the present study. An image was collected using *p*-polarized light, showing a large contrast between covered and bare regions at this value of θ_i . Rectangular regions of interest (ROIs) were then defined, corresponding to bare, patterned, and coated regions. Care was taken in choosing the borders of the ROIs; large signal fluctuations were obtained if an ROI border was on the edge of a feature or a heterogeneously covered region due to rounding errors in the calculated position of the ROI borders as θ_i was scanned.

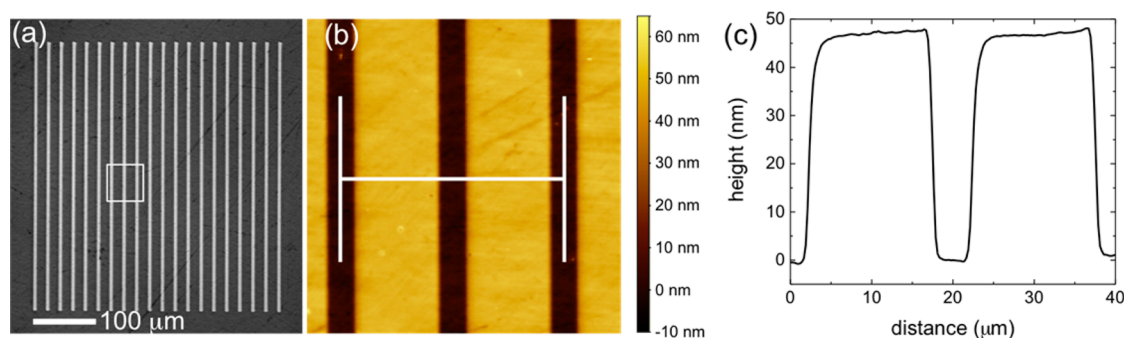


Figure 1. (a) Optical microscopy image of periodic channels patterned in a 48 nm thick PMMA film. The patterned region is $420 \times 400 \mu\text{m}$, and the channels have a period of $20 \mu\text{m}$. The white bar corresponds to a distance of $100 \mu\text{m}$. (b) Atomic force microscope topography image of the patterned channels within the white box shown in (a). (c) Line scan, averaged over a lateral distance of $30 \mu\text{m}$, perpendicular to the channels in the AFM image, corresponding to the white line shown in (b).

The time to collect a single SPR image was ~ 1 s. To collect a typical SPR curve, the angle of incidence was varied in steps of 0.1° over a range that was as small as 6° , but was typically 15° . Therefore, the time to collect a typical SPR curve was 1 s/image \times 150 images/scan, corresponding to the time to collect a single SPR curve of ~ 150 s = 2.5 min. This means that it is possible to track changes in thickness and roughness with characteristic timescales of ~ 10 min. During each scan, the new positions of the ROI borders and the average intensity within each ROI were calculated. Angular scans were also collected using *s*-polarized light. By dividing the *p*-polarized signal by the *s*-polarized signal, the SPR curves could be normalized, resulting in a signal that corresponded approximately to the reflectivity (R),²² and this signal has been plotted as the experimental SPR data in Figures 4–7. The division of the *p*-polarized signal by the *s*-polarized signal also reduced heterogeneities in illumination within the field of view (see the Supporting Information). Accounting for these heterogeneities is important since scanning the angle of incidence causes a shift in the location of each of the ROIs due to beam walking, which can produce significant artifacts in the SPR curve as the ROIs pass through heterogeneities in illumination.

For the patterned PMMA films containing one-dimensional channels, a single angular scan was performed with the plane of incidence parallel and perpendicular to the channels, using water at $T \sim 25^\circ\text{C}$ as the fluid medium. For cellulose microfibril-coated samples in aqueous buffer, measurements were performed at $T = 50^\circ\text{C}$ and angular scans were performed repetitively, allowing the kinetics of changes to the samples to be measured. At the beginning of each cellulose degradation experiment, angular scans were collected for 30–60 min prior to the introduction of the cellulolytic enzyme solution to allow the temperature to equilibrate. The enzyme solution was then added to the chamber, and angular scans were collected for several hours to track the degradation of the cellulose.

Data Analysis Procedure. The SPR curves measured on the patterned PMMA films and the cellulose microfibril-coated samples were interpreted in terms of basis sets of “ideal” SPR curves. The “ideal” SPR curves were calculated for *p*-polarized light using a multilayer model based on the Fresnel equations.^{3,16} For the patterned PMMA films, an SPR curve measured on a “bare gold” region (obtained by removing a region of a PMMA film using electron-beam lithography) was used to determine the best-fit values of thickness h_{Au} and index of refraction n_{Au} of the gold film and the index of refraction n_{med}

of the surrounding medium. An SPR curve measured on a region uniformly coated by the 48 nm thick PMMA film was used to determine the best-fit value of the index of refraction of n_{PMMA} . Using these best-fit parameter values, the series of “ideal” SPR curves was calculated for different uniform thicknesses of the PMMA layer, $h = \{0, 1, 2, \dots, 60\}$ nm. Any nonuniformity of the substrate (scratches, variations in metal layer thickness) will also change the shape of the measured SPR curves. To account for these nonuniformities, lines of constant reflectivity of -1 and 1 were added to the basis set. The sum of the resultant weights corresponding to the range of thicknesses included in the fit was then normalized to 1. A similar method was used for the cellulose microfibril-coated samples, except that the index of refraction for cellulose was fixed to a value of $n_{\text{cel}} = 1.4641$.²³

We performed the data analysis using a custom Matlab program in which the best fit to the SPR curve for the “bare gold” layer was calculated; the basis set of “ideal” SPR curves was then calculated, and then the basis set was used to calculate best fits to the experimental SPR curves of heterogeneously coated regions. We used the “lsqnonneg” function of Matlab in the least-squares fitting procedure, for which the fitting weights are constrained to be non-negative, since negative weights/coverage are not physical. This function allows the solution of problems of the form:

$$\min_x \|C \cdot x - d\|_2^2, \text{ with } x \geq 0$$

where C is the basis set of “ideal” curves, d is a vector containing the experimental curve, and x is a vector of the weights that fit the data. We chose this data fitting procedure because of the dramatic increase in the speed of the fitting procedure (by a factor of ~ 500) by using the “lsqnonneg” function of Matlab, in which the parameter values are constrained to be non-negative, compared to a conventional, iterative least-squares fitting approach. The use of this procedure, together with the use of a large number of basis SPR curves, leads to the “spiky” nature of the thickness histograms, but we stress that we are most interested in the average thickness and roughness values that are calculated from the thickness histograms, and these values are very robust with respect to the choice of the number/thickness of the slabs used to model the surface coating (Figure S7 of the Supporting Information).

RESULTS AND DISCUSSION

SPR Measurement of Samples with Idealized One-Dimensional Roughness. PMMA films with patterned periodic channels were used to probe the effects of an idealized, one-dimensional roughness on the SPRi experiments. Atomic force microscopy (AFM) imaging was used to determine the pitch, width, and depth of the channels in the patterned regions of the PMMA films. A representative optical microscopy image, an AFM topography image, and an AFM line scan measured perpendicular to the patterned channels are shown in Figure 1.

A histogram of the thickness values measured in the AFM topography image for an integer number of periods was constructed, and Gaussian peaks were fit to the peaks in the histogram (Figure 2). The ratio of the areas under the peaks in

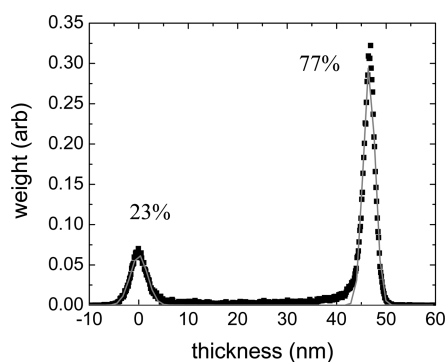


Figure 2. Histogram of average thickness values measured for an integer number of periods of AFM scans from Figure 1, as well as a fit of the histogram to two Gaussian peaks. The corresponding percentage areas under the peaks are labeled.

the histogram corresponding to the ratio of coated-to-bare areas agreed very well with that calculated from the AFM and optical microscopy images. The peaks in the histogram are likely broadened due to imperfections in the sample, as well as the noise associated with the AFM measurement.

An SPR curve for an ROI corresponding to the bare gold layer was analyzed to obtain the best-fit thickness and index of refraction values for the gold layer ($h_{\text{Au}} = 38.1 \text{ nm}$, $n_{\text{Au}} = 0.1509 + 5.0755i$) and the index of refraction of the water ($n_{\text{water}} = 1.3332$) (Figure S-1 of the Supporting Information). An SPR curve for an ROI corresponding to a uniformly coated region of the PMMA film was analyzed to determine the best-fit value of the index of refraction n_{PMMA} for the 48 nm thick PMMA layer (Figure S-2 of the Supporting Information). The set of best-fit parameters was then used to construct the basis set of “ideal” SPR curves, corresponding to different values of the thickness of the PMMA layer h_{PMMA} (Figure S-3 of the Supporting Information). In the basis set, the angle of the SPR minimum increases approximately linearly with increasing h_{PMMA} ($\sim 0.1^\circ/\text{nm}$, Figure S-4 of the Supporting Information), whereas the minimum intensity and width of the SPR dip are approximately constant.

Angle-scanning SPRi experiments were performed on the patterned PMMA film with the channels parallel to the plane of incidence, as shown schematically in Figure 3a (parallel geometry). We measured two distinct dips in the SPR curve (as can be seen in Figure 4a) that were attributed to plasmons traveling either within the channels (corresponding to zero PMMA thickness) or between the channels (corresponding to

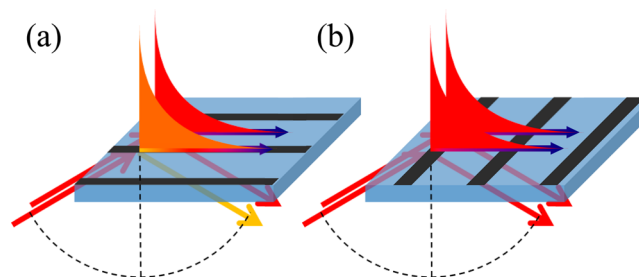


Figure 3. Schematic diagrams of the experimental geometries in which the surface plasmons travel (a) parallel and (b) perpendicular to the channels in the patterned PMMA samples (indicated by the black stripes). The incident and reflected beams are indicated as are the decays of the surface plasmons parallel and perpendicular to their propagation direction (indicated by blue arrows).

the original PMMA film thickness). The solid curve in Figure 4a was calculated using the distribution of thickness values obtained by performing a least-squares fit of the experimental SPR curve to the basis set of “ideal” SPR curves, with the weights within the distribution constrained to be non-negative. The best-fit distribution of thickness values is shown as red vertical bars in Figure 4b, together with the AFM thickness histogram from Figure 2 (black curve). In Figure S5 of the Supporting Information, we show the residuals, given by (measured reflectivity: best fit calculated reflectivity), for the SPR curves shown in Figures 4–7. It can be seen that the residuals are generally quite small ($< \pm 0.02$ in reflectivity for the residuals of Figure 4a) over the entire range of angles of incidence θ_i , indicating that the agreement between the measured and calculated SPR curves is very good.

Angle-scanning SPRi measurements were also performed on the same patterned PMMA film with the channels perpendicular to the plane of incidence, as shown schematically in Figure 3b. For this sample orientation, the surface plasmons travel through both covered and bare regions of the patterned sample as they decay (decay length of $\sim 20 \mu\text{m}$ along the propagation direction for $\lambda = 794.7 \text{ nm}$). The surface plasmons therefore sample an “average” PMMA thickness, producing a single dip in the SPR curve. The SPR curve measured for this sample orientation is shown in Figure 5a, together with the SPR curve calculated using the best-fit distribution of thickness values, which are in good agreement (residual plot shown in Figure S5b of the Supporting Information). The best-fit distribution of thickness values is shown as the red vertical bars in Figure 5b, together with the AFM thickness histogram from Figure 2 (black curve). The average thickness as measured by SPRi (vertical red bars in Figure 5b) is very close to the average thickness measured using AFM (vertical black line in Figure 5b).

The thickness histograms are necessarily “spiky” because of our use of the linear-algebra-based least-squares method to fit the data and the use of many more basis curves than are typically required to describe features in the data. The histograms would be less spiky if we were to use fewer slabs each with larger thickness, but this would not allow the description of sharp features in the data. Despite the “spiky” nature of the thickness histograms, we stress that the main purpose of the SPRi data fitting procedure is to determine the average sample thickness and roughness. Despite the spiky nature of the thickness histograms, the average thickness and roughness values have very little noise ($\sim 1\%$, as can be seen by

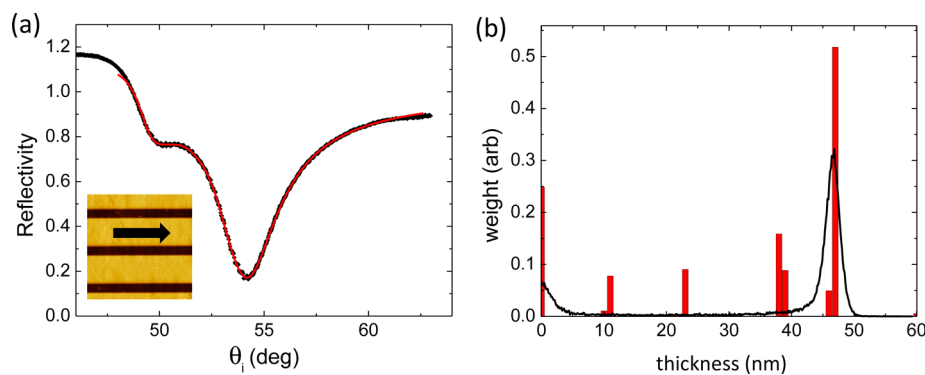


Figure 4. (a) Experimental SPR curve (black symbols) measured for a patterned PMMA film with channels parallel to the plane of incidence in the SPR experiment (as in Figure 3a), and the best fit curve (red line) calculated using a weighted superposition of the basis set of “ideal” SPR curves from Figure S-3 of the Supporting Information. (b) AFM thickness histogram from Figure 2 (black curve) and the relative weights of the best-fit set of “ideal” SPR curves (red bars) that were used to calculate the red curve in (a).

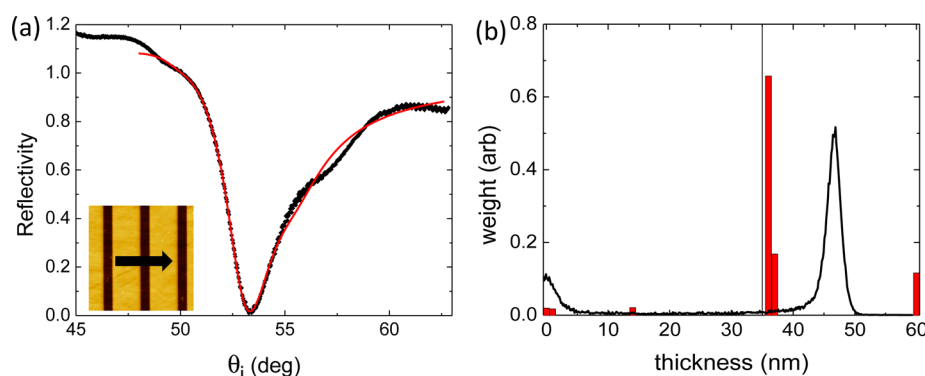


Figure 5. (a) Experimental SPR curve (black symbols) obtained for a patterned PMMA film with channels perpendicular to the plane of incidence in the SPR experiment and the best fit curve (red line) calculated using a weighted superposition of the basis set of “ideal” curves from Figure S-3 of the Supporting Information. (b) AFM thickness histogram from Figure 2 (black curve), and the relative weights of the best-fit set of “ideal” SPR curves (red bars) that were used to calculate the red curve in (a). The average thickness determined from the relative weights in the AFM thickness histogram is shown as a vertical black line.

the very small scatter in Figure 6, panels c and d, and Figure 7, panels c and d, shown below).

The use of the patterned PMMA film allowed us to explore in detail the effect of an idealized one-dimensional roughness on SPRi measurements. By fitting the experimental SPR curves to a basis set of “ideal” SPR curves corresponding to different layer thicknesses, we have obtained excellent agreement between the measured and best-fit SPR curves using a distribution of film thicknesses that is in agreement with that measured directly using AFM. In addition, by exploring the orientation of the surface plasmons relative to the one-dimensional roughness, we see that the SPR data is well-described by an average thickness for this case in which the length scale of the lateral roughness is significantly less than the decay length of the surface plasmons. We now apply this same procedure to a sample that has a much more disordered roughness: a cellulose microfibril-coated sample.

Enzymatic Degradation of Cellulose Microfibrils.

Representative SPR curves measured for a cellulose microfibril-coated ROI at different times of exposure to the enzyme cocktail solution are shown in Figure 6a. All of the SPR curves were analyzed to determine the corresponding distribution of cellulose microfibril thicknesses using the data analysis method described in the previous section. For these samples, a second basis set of “ideal” SPR curves of cellulose coatings of different thicknesses was constructed based on the analysis of a

thioglucose-covered gold ROI (with no cellulose) in buffer to determine (i) the effective complex index of refraction and the thickness of the thioglucose-covered gold layer, and (ii) the index of refraction of the buffer. A least-squares fit to each experimental SPR curve was performed to determine the best-fit weighted average of the “ideal” SPR curves, corresponding to different, uniform cellulose thicknesses, using an index of refraction for the cellulose coating of $n_{\text{cel}} = 1.4641$.²³ We note that, in our analysis of the data, the thickness of the coating includes a small contribution (approximately several nanometers) due to enzymes adsorbed onto the cellulose microfibrils and bare surface, where the index of refraction of the enzyme layer is assumed to be equal to that of the cellulose and is typical of a protein layer. The SPR curves calculated using the best-fit histograms of thicknesses are shown as solid lines in Figure 6a. The corresponding thickness histograms are shown in Figure 6b, which show the time evolution of the thickness profile after exposure to the enzyme cocktail solution. Two different measures of the average thickness and the roughness of the cellulose microfibril coatings, obtained from the SPR curves and the thickness histograms, are plotted as a function of time of exposure to the cellulolytic enzymes in Figure 6 (panels c and d).

In previous studies,^{5,13,14} only the angular position of the SPR minimum, which was interpreted as the average sample thickness, was tracked with time. In the present study, we

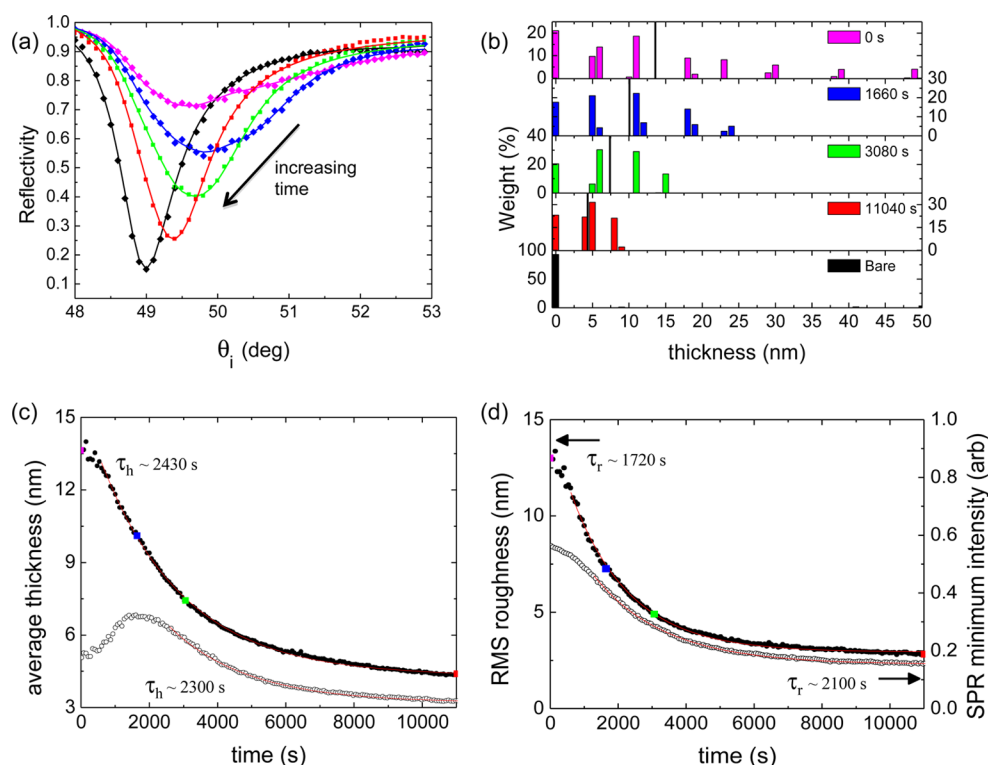


Figure 6. (a) Representative SPR curves of reflectivity versus angle of incidence θ_i for a cellulose microfibril-coated ROI at different times after exposure to a 20 $\mu\text{g/mL}$ enzyme cocktail solution. The experimental data are shown as solid symbols, and the solid curves were calculated using the best-fit thickness histograms shown in part (b). The different colors correspond to different times of exposure to the enzymes: $t = 0$ s (pink), $t = 1660$ s (blue), $t = 3080$ s (green), and $t = 11040$ s (red). The black data points correspond to a thioglucose-coated gold film in buffer before the introduction of the enzyme mixture from which the basis set of “ideal” SPR curves was generated. (b) Relative weights of the “ideal” SPR curves used to produce the best-fit curves in (a). For each time of exposure, the average thickness of the coating is indicated by a vertical black line. Dependence of (c) average thickness and (d) sample roughness on the time of exposure to the 20 $\mu\text{g/mL}$ enzyme cocktail solution for the same cellulose microfibril-coated ROI. Two different measures are provided in both (c) and (d): those obtained from the angular position and intensity of the SPR minimum are shown as hollow symbols, and those obtained from the best-fit thickness histograms in (b) are shown as solid symbols. Fits of ranges of the data to single exponentials are shown as thin solid red lines, and the corresponding best-fit values of the times of action τ_h (average thickness) and τ_r (roughness) are provided next to each data set. The colored symbols in (c) and (d) correspond to the data shown in parts (a) and (b).

obtained the same measure of the sample thickness (hollow symbols in Figure 6c), as well as another measure of the average sample thickness obtained from the average of the thickness histograms (solid symbols in Figure 6c). For samples with lateral thickness heterogeneities, the average sample thickness determined directly from the thickness histogram provides a better representation of the average sample thickness and its time evolution because it accounts explicitly for variations in thickness within the measured ROI. For the data shown in Figure 6, the average sample thickness obtained from the angular position of the SPR minimum is shifted at the beginning of the experiment because of the asymmetry of the SPR dip for the initially rough film (see Figure 6a) — contributions from thin areas are larger at large values of θ_i than contributions from thick areas at small values of θ_i . After a sufficiently long time of exposure to the enzymes, the sample roughness is small enough that the asymmetry of the SPR dip no longer skews the average value of the angular position of the SPR minimum, so that the two measures of the average sample thickness agree quite closely (to within 0.5 nm). It is not possible to provide a meaningful, direct comparison of the average thickness values determined by SPRi and AFM because of the highly nonuniform nature of the cellulose microfibril coating (see, for example, Figure S11 of the Supporting Information in ref 6) and the large difference in the lateral

resolution of the two techniques. For the data shown in Figure 6c, we have fit single exponential functions to ranges of the data for which the average thickness decreases monotonically with exposure time. This allowed us to obtain the times of action τ_h that characterize the decrease in the average thickness of the cellulose coating with exposure time to the cellulolytic enzymes: τ_h values of 2430 and 2300 s, which agree quite closely.

Because of the new data collection and analysis method introduced in the present manuscript, we were also able to track the roughness of the cellulose coating as enzymatic degradation proceeds. This provided an additional crucial piece of information that can help us to understand how the enzymes attack the cellulose microfibrils. The two roughness metrics are shown in Figure 6d, in which we compare a crude measure of the roughness, given by the intensity of the SPR minimum (hollow symbols), with a superior measure of the roughness, given by the RMS roughness calculated from the best-fit thickness histograms (solid symbols). The intensity of the SPR minimum provides a measure of the sample roughness in the following way: sample roughness will broaden the SPR dip, with a corresponding decrease in the depth of the SPR minimum, which we can use as a crude measure of the spread in thickness values (i.e., sample roughness). The more direct and reliable measure of the sample roughness provided by the

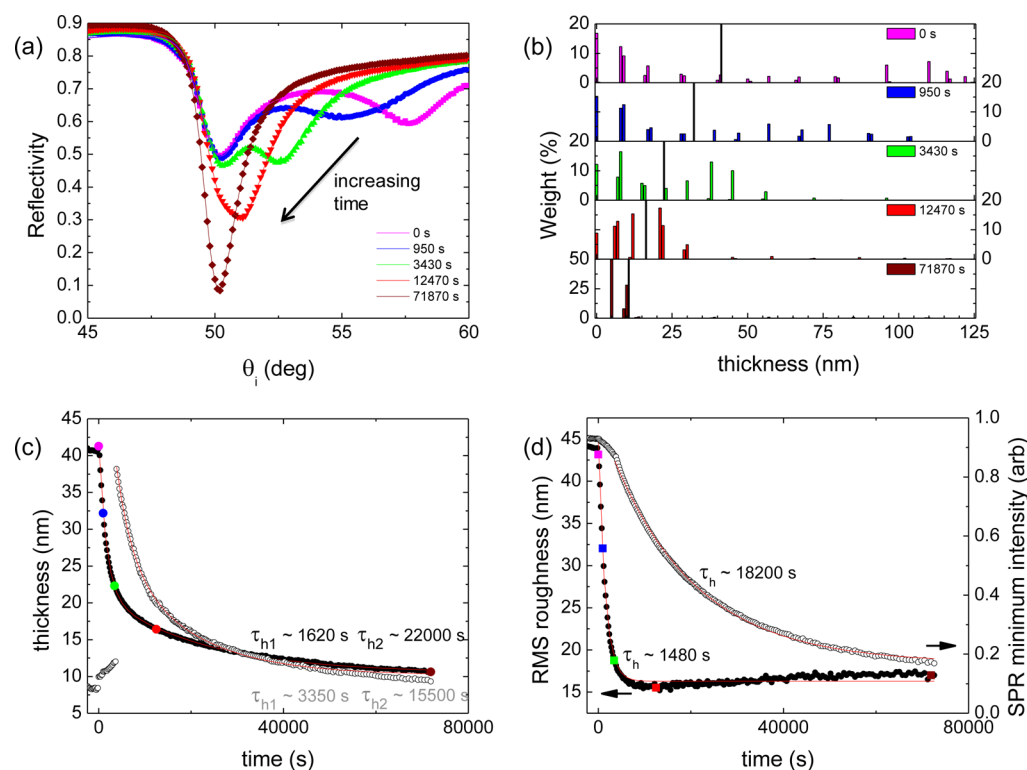


Figure 7. (a) Representative SPR curves of reflectivity versus angle of incidence θ_i for a cellulose microfibril-coated ROI at different times after exposure to a 21 $\mu\text{g/mL}$ CBH2 enzyme solution. The experimental data are shown as solid symbols, and the solid curves were calculated using the best-fit thickness histograms shown in part (b). The different colors correspond to different times of exposure to the enzymes: $t = 0$ s (pink), $t = 950$ s (blue), $t = 3430$ s (green), $t = 12470$ s (red), and $t = 71870$ s (brown). (b) Relative weights of the “ideal” SPR curves used to produce the best-fit curves in (a). For each time of exposure, the average thickness of the coating is indicated by a vertical black line. Dependence of (c) average thickness and (d) sample roughness on the time of exposure to the 21 $\mu\text{g/mL}$ CBH2 enzyme solution for the same cellulose microfibril-coated ROI. Two different measures are provided in both (c) and (d): those obtained from the position and intensity of the SPR minimum are shown as hollow symbols, and those obtained from the best-fit thickness histograms in (b) are shown as solid symbols. Fits of ranges of the data to (c) double exponentials and (d) single exponentials are shown as thin solid red lines, and the corresponding best-fit values of the times of action τ_h (average thickness) and τ_r (roughness) are provided next to each data set. The colored symbols in (c) and (d) correspond to the data shown in parts (a) and (b).

RMS roughness (solid symbols in Figure 6d) decreased rapidly from an initial value of 13.0 nm to an asymptotic value of ~ 2.8 nm with a characteristic time of action τ_r of 1720 s.

The effect of nonuniform coverage of the substrate can be much more dramatic than that shown in Figure 6. In Figure 7, we show data collected for a ROI on a very rough cellulose microfibril layer for which two distinct SPR dips are observed at the beginning of the experiment (pink curve). The low-angle SPR dip corresponds to relatively low coverage (very close to bare substrate), and the high-angle SPR dip corresponds to relatively high coverage. These two SPR dips correspond to two distinct distributions of peaks in the thickness histograms in Figure 7b: one distribution centered approximately at zero thickness and the other distribution centered at approximately 100 nm. As degradation proceeds, the angular position of the high-angle SPR dip decreases continuously toward the bare surface curve, as can be seen in the SPR curves and the thickness histograms in Figure 7 (panels a and b). If we compare the two measures of the sample thickness, as shown in Figure 7c, a discontinuous jump is observed at an exposure time of ~ 6000 s in the typical thickness measure corresponding to the SPR dip angle (hollow symbols in Figure 7c). Clearly, this does not correspond to a discontinuous jump in the average thickness but rather to a shift in the global minimum in reflectivity from the low-angle SPR dip to the high-angle SPR

dip at this value of the exposure time. In contrast, the average thickness determined from the thickness histograms (solid symbols in Figure 7c) shows a continuous decrease with exposure time and is a much more accurate measure of the average sample thickness. We note that a small spike in thickness can be seen at $t = 0$ (e.g., pink data point), corresponding to the small increase in thickness (~ 1 nm) associated with the initial adsorption of enzymes. In addition, there is a large discrepancy for the two measures of the sample roughness. The RMS roughness determined from the thickness histograms shows a much more dramatic decrease in roughness with exposure time, corresponding to relatively quick decreases in the average value and breadth of the thickness distributions in Figure 7b. This example of very nonuniform coverage clearly illustrates the advantage of the new analysis method in tracking changes in average thickness and roughness for rough samples.

Collectively, the measured decreases in the average thickness and RMS roughness of the cellulose microfibril coating with time of exposure to the enzyme cocktail solution indicated that enzymatic degradation proceeded with a relatively rapid decrease in the roughness of the coating, as the average thickness decreased more slowly with time of exposure.

SUMMARY AND CONCLUSIONS

We have extended the technique of angle-scanning surface plasmon resonance imaging (SPRi) to allow the determination of the distribution of thicknesses present in laterally heterogeneous coatings. This is possible because of improvements in the experimental procedures and the implementation of a novel data analysis method. The data analysis method involves modeling the rough films as a linear combination of uniform layers of different thickness and performing a linear-algebra-based least-squares fit of the measured SPR curves to a basis set of "ideal" SPR curves corresponding to different uniform thicknesses. This allows the determination of a best-fit histogram of thickness values for the rough film that can be used to determine the average thickness and RMS roughness of the film. We have tested this procedure using PMMA films with patterned periodic channels that provided an idealized form of one-dimensional roughness. SPRi measurements performed parallel and perpendicular to the patterned channels show excellent agreement with the SPR curves calculated using the best-fit histogram of thickness values and the average film thickness as measured using AFM, respectively.

We have applied the data analysis method to heterogeneous coatings of cellulose microfibrils to track the thickness and RMS roughness of the coatings as a function of time of exposure to cellulolytic enzymes. This has allowed us to obtain a direct measure of the characteristic times of action of the enzymes associated with changes in the average film thickness and RMS roughness, providing useful metrics of enzyme activity on cellulose microfibrils that are of direct interest to the cellulosic ethanol industry.

ASSOCIATED CONTENT

Supporting Information

Additional information as noted in text. This material is available free of charge via the Internet at <http://pubs.acs.org>.

AUTHOR INFORMATION

Corresponding Author

*E-mail: dutcher@uoguelph.ca. Tel: 519-824-4120, ext. 53950. Fax: 519-836-9967.

Notes

The authors declare no competing financial interest.

ACKNOWLEDGMENTS

This work was supported by an NSERC Collaborative Research and Development Grant to A.J.C., J.L., and J.R.D., in collaboration with Iogen Corporation, and NSERC Discovery Grants to A.J.C., J.L., and J.R.D. We acknowledge useful discussions with Chris Hill and Oleh Tanchak, and we are grateful to Jay Leitch for assistance with the operation of the SEM. J.R.D. and J.L. acknowledge Canada Research Chair Awards.

REFERENCES

- (1) Schasfoort, R. B. M.; Tudos, A. J. *Handbook of Surface Plasmon Resonance*; Royal Society of Chemistry: London, 2008.
- (2) Homola, J.; Piliarik, M. In *Surface Plasmon Resonance Based Sensors*; Homola, J., Ed.; Springer Series on Chemical Sensors and Biosensors; Springer: Berlin, 2006; pp 45–67.
- (3) Raether, H. *Surface Plasmons on Smooth and Rough Surfaces and on Gratings*; Springer: Berlin, 1988.
- (4) Brockman, J. M.; Nelson, B. P.; Corn, R. M. *Annu. Rev. Phys. Chem.* **2000**, *51*, 41–63.

- (5) Ahl, S.; Cameron, P.; Liu, J.; Knoll, W.; Erlebachner, J.; Yu, F. *Plasmonics* **2008**, *3*, 13–20.
- (6) Allen, S. G.; Tanchak, O. M.; Quirk, A.; Raegen, A. N.; Reiter, K.; Whitney, R.; Clarke, A. J.; Lipkowski, J.; Dutcher, J. R. *Anal. Methods* **2012**, *4*, 3238–3245.
- (7) Jiang, G.; Baba, A.; Ikarashi, H.; Xu, R.; Locklin, J.; Kashif, K. R.; Shinbo, K.; Kato, K.; Kaneko, F.; Advincula, R. J. *Phys. Chem. C* **2007**, *111*, 18687–18694.
- (8) Kang, T.; Hong, S.; Choi, I.; Sung, J. J.; Kim, Y.; Hahn, J.-S.; Yi, J. *J. Am. Chem. Soc.* **2006**, *128*, 12870–12878.
- (9) Golden, M. S.; Bjonnes, A. C.; Georgiadis, R. M. *J. Phys. Chem. C* **2010**, *114*, 8837–8843.
- (10) Lyon, L. A.; Peña, D. J.; Natan, M. J. *J. Phys. Chem. B* **1999**, *103*, 5826–5831.
- (11) Štěpánek, J.; Vaisocherová, H.; Piliarik, M. In *Surface Plasmon Resonance Based Sensors*; Homola, J., Ed.; Springer Series on Chemical Sensors and Biosensors; Springer: Berlin, 2006; pp 69–91.
- (12) Piliarik, M.; Homola, J. In *Surface Plasmon Resonance Based Sensors*; Homola, J., Ed.; Springer Series on Chemical Sensors and Biosensors; Springer Berlin Heidelberg, 2006; pp 95–116.
- (13) Beusink, J. B.; Lokate, A. M. C.; Besselink, G. A. J.; Puijn, G. J. M.; Schasfoort, R. B. M. *Biosens. Bioelectron.* **2008**, *23*, 839–844.
- (14) Chegel, V.; Chegel, Y.; Guiver, M. D.; Lopatynskiy, A.; Lopatynska, O.; Lozovski, V. *Sens. Actuators, B* **2008**, *134*, 66–71.
- (15) Kolomenski, A.; Kolomenskii, A.; Noel, J.; Peng, S.; Schuessler, H. *Appl. Opt.* **2009**, *48*, 5683–5691.
- (16) Homola, J. In *Surface Plasmon Resonance Based Sensors*; Homola, J., Ed.; Springer Series on Chemical Sensors and Biosensors; Springer: Berlin, 2006; pp 3–44.
- (17) Fenstermaker, C. A.; McCrackin, F. L. *Surf. Sci.* **1969**, *16*, 85–96.
- (18) Quirk, A.; Lipkowski, J.; Vandenende, C.; Cockburn, D.; Clarke, A. J.; Dutcher, J. R.; Roscoe, S. G. *Langmuir* **2010**, *26*, 5007–5013.
- (19) Kycia, A. H.; Sek, S.; Su, Z.; Merrill, A. R.; Lipkowski, J. *Langmuir* **2011**, *27*, 13383–13389.
- (20) Wang, J.; Quirk, A.; Lipkowski, J.; Dutcher, J. R.; Hill, C.; Mark, A.; Clarke, A. J. *Langmuir* **2012**, *28*, 9664–9672.
- (21) Ruemmele, J. A.; Golden, M. S.; Gao, Y.; Cornelius, E. M.; Anderson, M. E.; Postelnicu, L.; Georgiadis, R. M. *Anal. Chem.* **2008**, *80*, 4752–4756.
- (22) Berger, C. E. H.; Kooyman, R. P. H.; Greve, J. *Rev. Sci. Instrum.* **1994**, *65*, 2829–2836.
- (23) Kasarova, S. N.; Sultanova, N. G.; Ivanov, C. D.; Nikolov, I. D. *Opt. Mater.* **2007**, *29*, 1481–1490.